

## Article

# Optimal Design and Analysis for a New 1-DOF Compliant Stage Based on Additive Manufacturing Method for Testing Medical Specimens

Minh Phung Dang <sup>1</sup>, Hieu Giang Le <sup>1</sup>, Nguyen Thanh Duy Tran <sup>1</sup>, Ngoc Le Chau <sup>2</sup> and Thanh-Phong Dao <sup>3,4,\*</sup> 

- <sup>1</sup> Faculty of Mechanical Engineering, Ho Chi Minh City University of Technology and Education, Ho Chi Minh City 700000, Vietnam; phungdm@hcmute.edu.vn (M.P.D.); gianglh@hcmute.edu.vn (H.G.L.); 17143006@student.hcmute.edu.vn (N.T.D.T.)
- <sup>2</sup> Faculty of Mechanical Engineering, Industrial University of Ho Chi Minh City, Ho Chi Minh City 700000, Vietnam; chaungocle@iuh.edu.vn
- <sup>3</sup> Division of Computational Mechatronics, Institute for Computational Science, Ton Duc Thang University, Ho Chi Minh City 700000, Vietnam
- <sup>4</sup> Faculty of Electrical & Electronics Engineering, Ton Duc Thang University, Ho Chi Minh City 700000, Vietnam
- \* Correspondence: daothanhhong@tdtu.edu.vn

**Abstract:** In situ nanoindentation is extensively employed for online observing deformation and mechanical behaviors of bio-materials. However, the existing designs of the positioning stages have limited performances for testing soft or hard biomaterials. Consequently, this paper proposes a new structural design of a compliant one degree of freedom (01-DOF) stage with faster response. In addition to a new design, this article applies an analytical method to estimate the kinematic and dynamic behaviors of the stage. Firstly, the 01-DOF stage is designed with two modules, including a displacement amplifier with six levers and a symmetric parallelogram mechanism. Secondly, a kinetostatic diagram of the stage is built by pseudo-rigid-body method. Then, the dynamic equation of the proposed stage is formulated using the Lagrange method. In order to speed up the response of the indentation system, the structural optimization of the stage is conducted via the Firefly algorithm. The results showed that the theoretical first-order resonant frequency is found at about 226.8458 Hz. The theoretical consequences are nearby to the verified simulation. Besides, this achieved frequency of the presented stage is greater than that of previous stages. In an upcoming study, the prototype will be fabricated by additive manufacturing method or a computerized wire cutting method in order to verify the analytical results with experimental results.

**Keywords:** compliant mechanism; 1-dof stage; in-situ nanoindentation; pseudo-rigid-body model; Lagrange's principle; Firefly algorithm



**Citation:** Dang, M.P.; Le, H.G.; Tran, N.T.D.; Chau, N.L.; Dao, T.-P.

Optimal Design and Analysis for a New 1-DOF Compliant Stage Based on Additive Manufacturing Method for Testing Medical Specimens. *Symmetry* **2022**, *14*, 1234. <https://doi.org/10.3390/sym14061234>

Academic Editor: Jan Awrejcewicz

Received: 3 May 2022

Accepted: 10 June 2022

Published: 14 June 2022

**Publisher's Note:** MDPI stays neutral with regard to jurisdictional claims in published maps and institutional affiliations.



**Copyright:** © 2022 by the authors. Licensee MDPI, Basel, Switzerland. This article is an open access article distributed under the terms and conditions of the Creative Commons Attribution (CC BY) license (<https://creativecommons.org/licenses/by/4.0/>).

## 1. Introduction

Generally, in situ nanoindentation devices use mechanical components for online detecting and observing of the deformable mechanics and mechanical properties of bio-materials [1]. In particular, in situ nanoindentation was applied in the field of implants (e.g., bone, teeth, femur, prosthetics) [2,3]. However, the mechanical components, (e.g., machine base, shaft, bush, gear, cam, sliding rail, ball screw, and ball nut) have existing restrictions, such as clearance, friction, wear, and vibration. Consequently, these mechanical devices are complicated for obtaining a precise transmission. In addition, a compact structure is a recent tendency in designing a new in situ nanoindentation tester in order to reduce energy consumption. Especially, in situ nanoindentation often requires many force and displacement feedback sensors to achieve a precise positioning capability. In such in situ nanoindentation applications, the two main modules consist of an indenter driving stage and a bio-material sample locating stage. However, the existing stages still have a slow responding speed, i.e., low resonant frequency [4,5]. Additionally, they are difficult to

install positioners in in situ nanoindentation with a scanning electron microscope (SEM) or transmission electron microscope (TEM) due to their large size. Therefore, a new structural design of the stage with a faster responding speed has an increasing demand.

In the two last decades, many designs of in situ nanoindentation in SEM/TEM were developed. Rabe et al. [6] developed an SEM nanoscratch instrument with the indenter driving stage of 20  $\mu\text{m}$ . A TEM nanoindentation was proposed for deformation testing of Al–Mg films [7]. Considering the mechanical and electrical properties of nanomaterials, a survey on SEM in situ nanoindentation was investigated deeply [8]. The nanomechanical properties of micro/nano materials were observed through in situ nanoindentation in SEM [9]. Nano thin-films for an MEM force sensor were tested by in situ nanoindentation in SEM and TEM [10]. One-D nanostructure materials were checked via this technique [11]. Presently, according to the crucial benefits of compliant mechanisms include smooth motion without friction and backlash, monolithic structure, slight mass, cheap price and miniature structure [12–14], it has been expansively utilized to research and gradually substitute conventional structure. Particularly for the nanoindentation tester, an indenter driving stage of 11.44  $\mu\text{m}$  was developed by Huang [15]. Additionally, Huang et al. [16] developed another stage with 40  $\mu\text{m}$ . Besides, Zhao et al. [17] developed an indenter driving stage with 15  $\mu\text{m}$ . In practical applications, a nanoindentation device requires an excellent locating precision, high operating travel and a high material strength [15,18].

Along with the applications in in situ nanoindentation, compliant mechanisms have been extensively exploited for prospective applications, e.g., positioner [19], lithography [20], microscopy [21], and micromanipulator [22]. Specifically, a diamond turning operation was developed using a compliant mechanism [23]. Several compliant reconfigurable stages were developed in a module architecture [24]. The compliant mechanism was applied for polishing operations [25]. However, the stroke of a piezoelectric actuator is often small. In order to obtain the larger working travels, the previous stage was integrated with displacement amplifiers [26]. An effective design of a 3-DOF positioner with a lever amplifier type was well developed [7]. Then, a two-lever displacement magnification mechanism was proposed [27]. A hybrid lever-bridge amplifier was designed [28]. A Scott–Russell mechanism was used as a displacement amplifier [29]. In the design synthesis of compliant mechanisms, formulating modeling approaches in predicting the mechanical behaviors is often complex because the kinematic and mechanical behaviors are coupled, i.e., these behaviors are ambiguous. At present, modeling compliant mechanisms is conducted in two main approaches. Primarily, analytical approaches comprise of a pseudo-rigid-body model (PRBM), compliance matrix method, elastic beam theory, and Castigliano's second theorem [30]. Besides, intelligence-based computational methods were well-formulated such as fuzzy logic, artificial neural network, and adaptive neuro-fuzzy inference system (ANFIS) [31]. Especially, the PRBM is well blended with the Lagrange method to rapidly assess the primary superiority performances of the positioners, e.g., force-displacement curve and dynamic response.

Although many micro/nanopositioners have been dedicated for ultra positioning engineering but there has been lack of studies on the precision stages for driving the indenter which can be embedded into the nanoindentation tester for biomedical samples (e.g., bone, teeth, femur implants). Additionally, the working travel for stages for driving the indenter is still small and they are difficult to apply for a diverse variety of many nanoindentation applications. With the purpose of fulfilling the technical demands for an in situ nanoindentation, a miniaturized size, a fast response, and an effective computation method of the indentation should be balanced. In other words, the symmetry in designing and analyzing phases of indentation should remain to reduce the complexity of the design and facilitate more effective computation techniques. Therefore, the present paper proposes a new design of the stage/positioner with one degree of freedom (1-DOF). The stage is created based on a displacement amplifier with six levers and a symmetric parallelogram mechanism to achieve a high output displacement and reduce parasitic motion error for indenting a material specimen, especially a bio-specimen. The new novelties of this

article are summarized as follows: (i) A new design of a compliant 01-DOF stage with a good dynamic performance in bio-specimen nanoindentation application. (ii) An new optimization design and synthesis approach that is proposed based on the PRBM, Lagrange, and Firefly algorithm to improve the quality response of the 01-DOF stage.

This article is motivated to develop a new design for the 1-DOF stage. The stage is built by integrating the six-lever displacement amplifier and the parallel driving mechanism. First of all, the kinematic and dynamic equations are established using a combination of PRBM and Lagrange method. Then, according to established analytical equations, the Firefly algorithm is utilized to enhance the frequency of the proposed stage.

## 2. Conceptual Design of Compliant 1-DOF Stage

In our previous research [32], a potential application of the compliant 1-DOF stage, or the so-called Z-positioning stage, is shown in Figure 1. The coarse Z-axis positioner, a coarse XY-positioner, an XY-fine positioner, and a fine Z-axis positioner are among the main components of the system. The coarse XY positioner is used to determine an initial location of a bio-specimen, the XY-fine stage is used to define fine location, and the coarse Z-axis positioner is used to move the testing bio-specimen toward the indenter. Eventually, the 1-DOF positioner is used to drive the indenter to the checking specimen. In the present article, the compliant 1-DOF stage is developed for such a nanoindentation system.

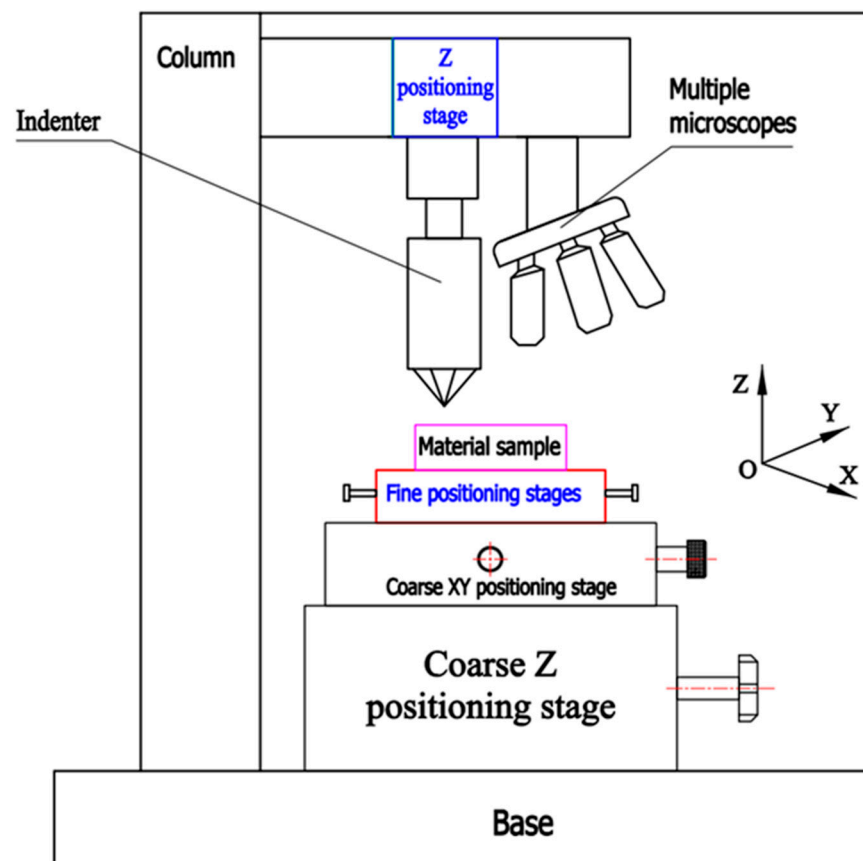


**Figure 1.** A scheme of proposed nanoindentation [32].

In this work, the lever amplifier is aimed to enlarge the displacement of the stage. Figure 2 describes a basic lever mechanism. Specifically, point O indicates a fixed link which presents for the lever rotation location. Additionally, the input position and the output position are noted as P and Q, respectively. The operating principle of an amplifier comprises of the following steps: (i) an input displacement  $y_1$  affects at point M, the lever revolves an angle  $\varphi$ . Subsequently, the position Q transfers to Q' in order to obtain the

deformation  $y_2$ . Meanwhile, the one-lever amplifier causes a significant decoupling error. Consequently, to decrease the decoupling error and enhance the output displacement, a symmetric six-lever displacement amplifier is monolithically designed in the proposed positioner, as illustrated in Figure 3. Moreover, a combination of the symmetric six-leaf parallel mechanism and the amplifier is to decline the parasitic motion error, as shown in Figure 4. Especially, this guiding mechanism significantly reduces the parasitic motion error for the compliant 01-DOF positioner. Based on the working principle, the amplifying ratio are approximately obtained:

$$r_{lever} = y_2/y_1 = x_2/x_1 \quad (1)$$

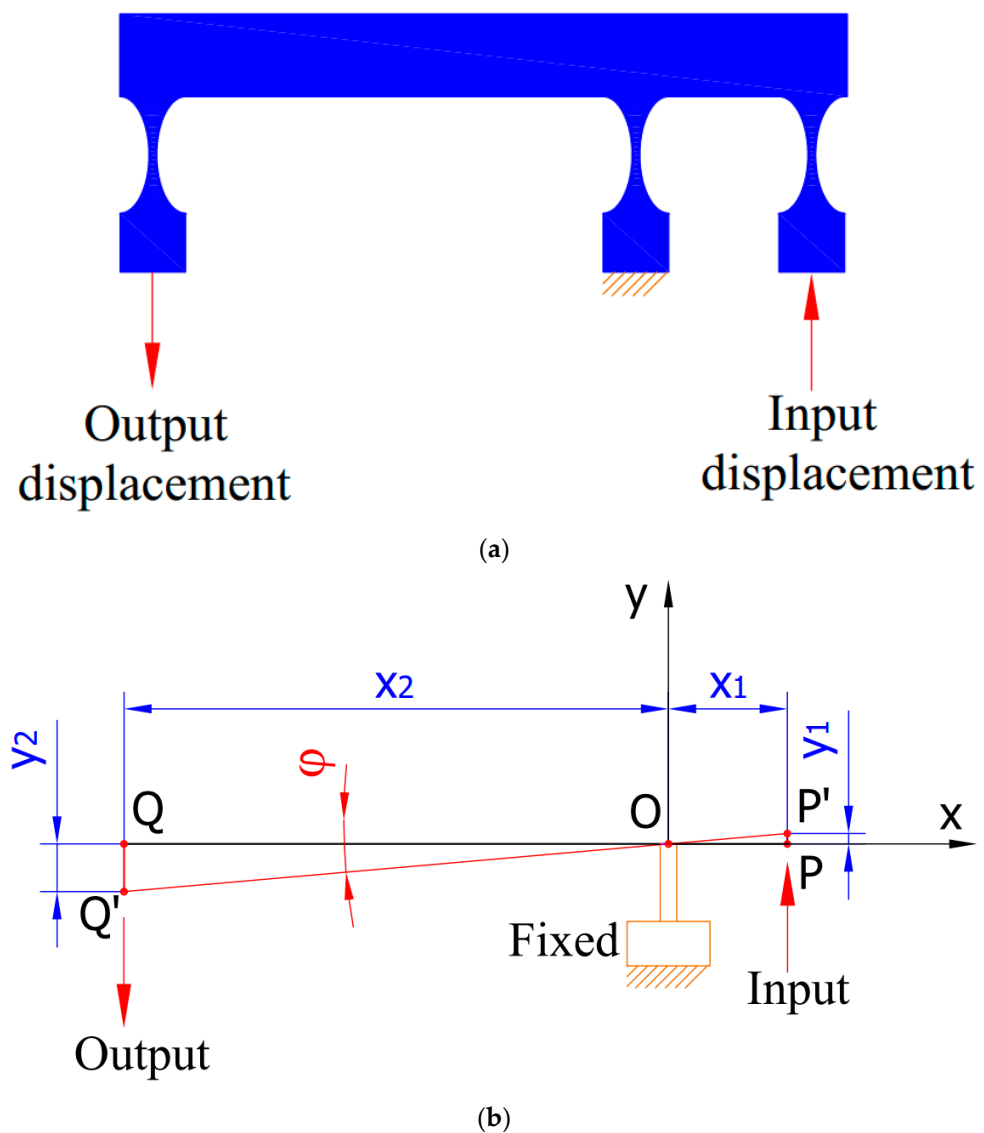


**Figure 2.** Schematic: (a) A lever displacement amplifier, (b) amplification ratio.

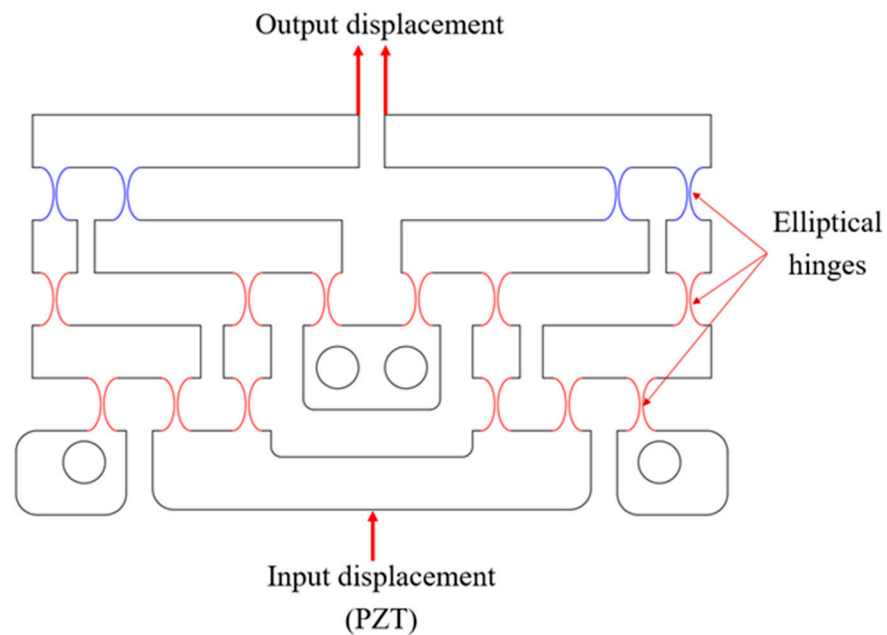


**Figure 3.** A six-level displacement amplifier with elliptical hinges.

In Figure 4, the displacement amplifier includes three floors with six levers which are employed to enlarge the working displacement of the stage. Specifically, the number of odd floors ensures that the input displacement has the same direction with the output displacement. For this purpose, controlling the number of floors will ensure the amplification ratio and the direction of the output displacement in order to effectively monitor the indentation process. Meanwhile, the parallel guiding mechanism that consists of six leaf hinges, which is aimed to generate the translation motion, i.e., eliminated parasitic motion errors from the remaining (x and y) axes. It consists of a lever amplification mechanism of floor 1 (LAM #1), lever amplification mechanism of floor 2 (LAM #2), and lever amplification mechanism of floor 3 (LAM #3). The input is acted via a piezoelectric actuator (PZT).

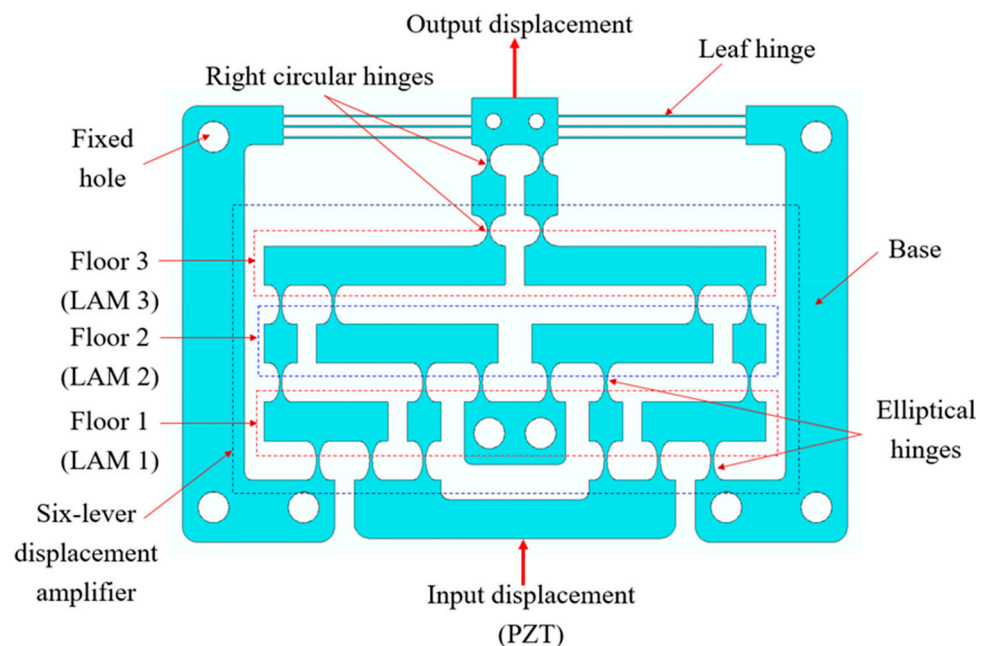


**Figure 4.** Proposed compliant 1-DOF stage.

The material of the proposed 01-DOF stage was manufactured by material Al-7075 because of its outstanding properties of this material. The 01-DOF stage comprises of: (i) fixed holes, (ii) a PZT actuator, (iii) a parallel guiding mechanism, and (iv) a six-lever displacement amplifier. The sum dimensions of the stage are around  $171 \text{ mm} \times 108 \text{ mm} \times 10 \text{ mm}$ . The elliptical hinge was chosen for the stage due to its excellent benefits [33]. Figure 5 shows the dimensional diagram of the stage. Table 1 provides the key dimensions of the stage. Specifically,  $G$  is the thickness of the elliptical hinge of the LAM #1 and LAM #2,  $R$  is the thickness of the elliptical hinge of the LAM #3,  $S$  is the thickness of the right circular hinge of the output end, and  $U$  is the thickness of the leaf hinge of the output end.

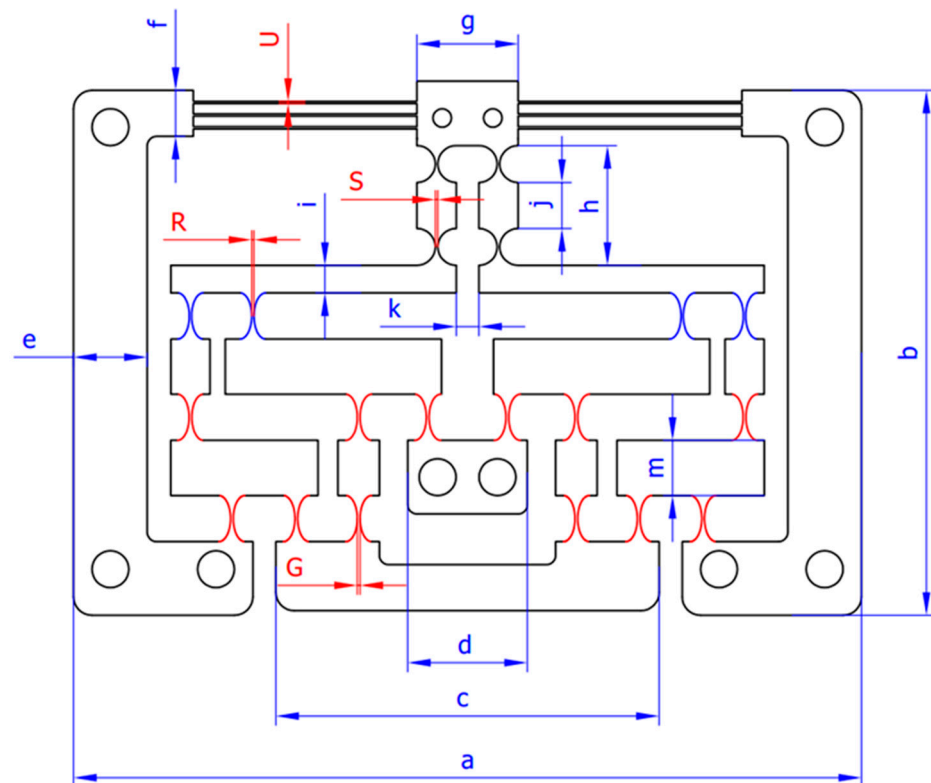


**Figure 5.** Dimensional schematic of the proposed stage.

**Table 1.** Dimensional factors of the proposed stage.

Symbol	Value	Symbol	Value	Unit
$a$	171	$i$	6	mm
$b$	108	$j$	10	mm
$c$	82	$k$	5	mm
$d$	26	$m$	12	mm
$e$	16	$G$	$0.65 \leq G \leq 0.75$	mm
$f$	10	$R$	$0.5 \leq R \leq 0.7$	mm
$g$	22	$S$	$0.5 \leq S \leq 0.65$	mm
$h$	26	$U$	$0.5 \leq U \leq 0.6$	mm

### 3. Proposed Method

The stage is designed according to the multi-lever amplifier and the parallelogram mechanism. Then, an analytical modelling is performed via the combination of PRBM and Lagrange to establish the dynamic equation of the stage. The flowchart of the proposed optimization approach for the stage is illustrated in Figure 6. It is briefly summarized as follows.

- A conceptual design of the 1-DOF stage is predetermined, i.e., built kinematic scheme.
- Predetermine the technical specifications for the 1-DOF stage.
- Establish the dynamic equation for the 1-DOF stage by developing the PRBM and Lagrange's method.
- Verify the theoretical results by using ANSYS software.
- If the mathematical models are corrected, the process moves to next step. Otherwise, the process turns back the step 1.
- Determine the design variables, objective function, and constraint function.
- Firefly algorithm is utilized for the dynamic response of the proposed stage.
- The optimal results are verified via simulations in ANSYS software.
- The first frequency of the stage is compared with that from the previous studies.

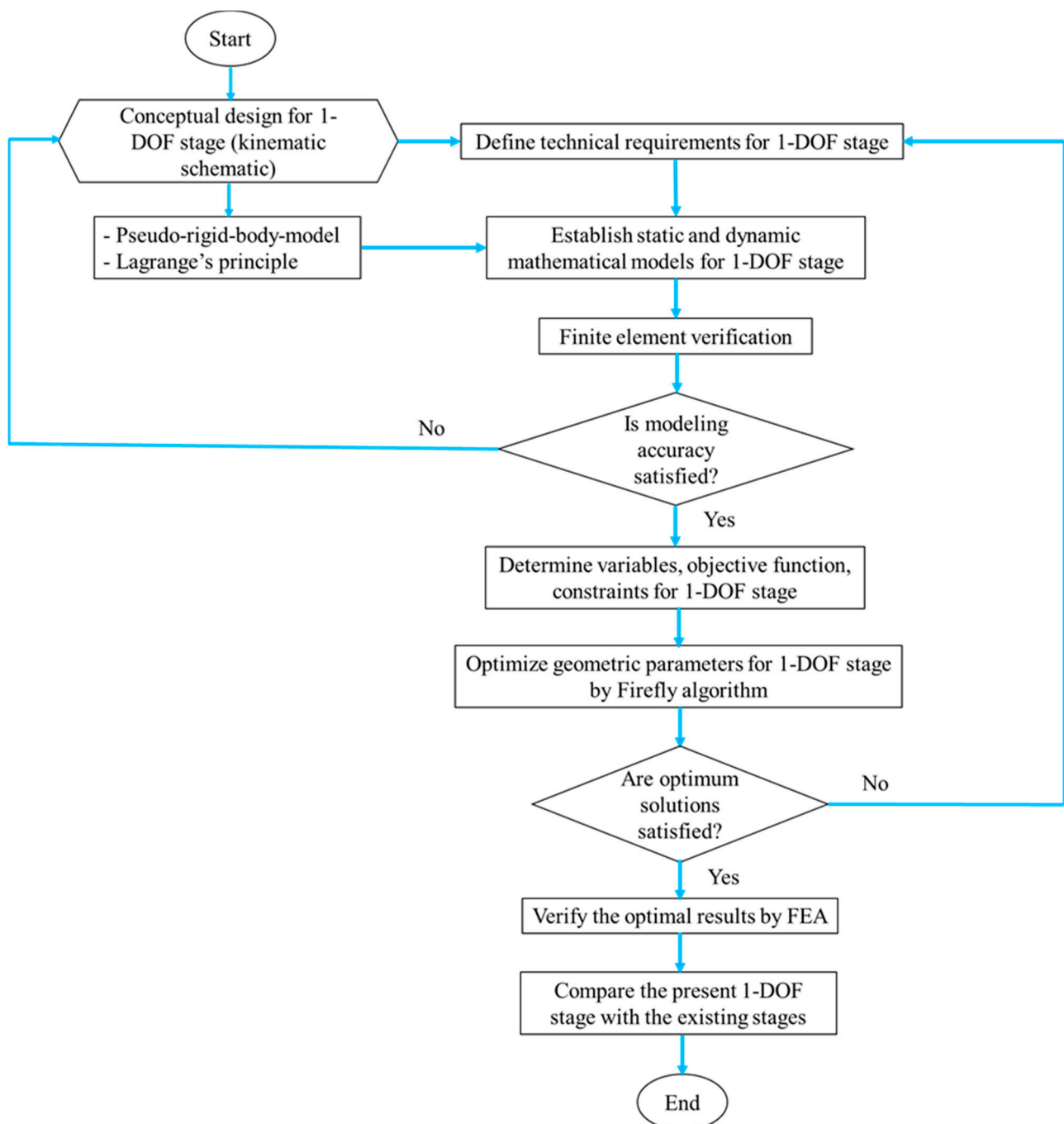


**Figure 6.** Flowchart of proposed optimization method for 1-DOF stage.

### 3.1. Overview of Pseudo-Rigid-Body Method

The PRBM is applied to rapidly evaluate the characteristics of the stage. Figure 7a,b indicates a beam and its PRBM. A torsional spring is located at the beam. The main problem precisely locates the pivot, and the spring stiffness is correctly calculated when the beam is subjected to two external loads (force  $F$  and moment  $M$ ). The details of PRBM can be found in [30].

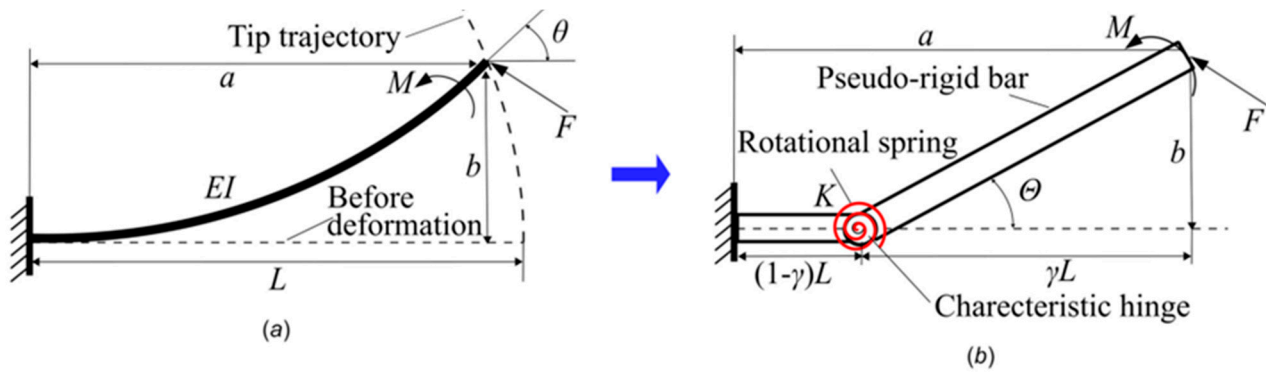


Figure 7. PRBM of a beams [30]: (a) beam and (b) its PRBM [30].

### 3.2. Lagrange's Principle

The 1-DOF stage is expected to achieve a high speed, i.e., the first frequency should be high. Consequently, the determination of the dynamic equation is essential for designing controllers later. To conclude, the Lagrange approach was chosen for this study. The details of Lagrange is described in [30].

The first-order natural frequency ( $f$ ) is proportional to the angular velocity of the system and the frequency can be computed by:

$$f = \frac{\omega}{2\pi}, \quad (2a)$$

$$f = \frac{\sqrt{K/M}}{2\pi}. \quad (2b)$$

The kinetic energy ( $V$ ) is calculated as:

$$V = \frac{1}{2}k_{eq}d^2, \quad (3)$$

The potential energy ( $T$ ) is computed by:

$$T = \frac{1}{2}m_{eq}\dot{d}^2, \quad (4)$$

where  $d$  denotes the input displacement,  $k_{eq}$  depicts the equivalent input stiffness, and  $m_{eq}$  is the equivalent mass.

The PRBM-based Lagrange method is applied to build the dynamics. The equation of Lagrange is briefly formed as:

$$\frac{d}{dt} \frac{\partial T}{\partial \dot{d}} - \frac{\partial T}{\partial d} + \frac{\partial V}{\partial d} = F_a. \quad (5)$$

where  $V$  represents the kinetic energy,  $T$  denotes the potential energy, and  $F_a$  is the generalized force.

### 3.3. Firefly Algorithm

The Firefly algorithm [34] was selected for maximizing the frequency due to its intelligent behaviors; the Firefly algorithm (FA) was proposed by Yang [34]. This optimizer was motivated by the flashing nature of fireflies. The firefly's flash is exploited as a signal to fascinate other fireflies. The algorithm had three regulations: (i) the total number of fireflies are unisexual, and one firefly are fascinated by all the other fireflies. (ii) Fascination is proportionate to the brightness. Hence, the less bright one goes to the brighter one. (iii) If there are not any fireflies that are brighter than a specified firefly, it goes to travel arbitrarily. The brilliance should be related with the objective function. According to above-mentioned regulations, the flowchart of this algorithm is exhibited in Figure 8. The details of FA can be found in [34].

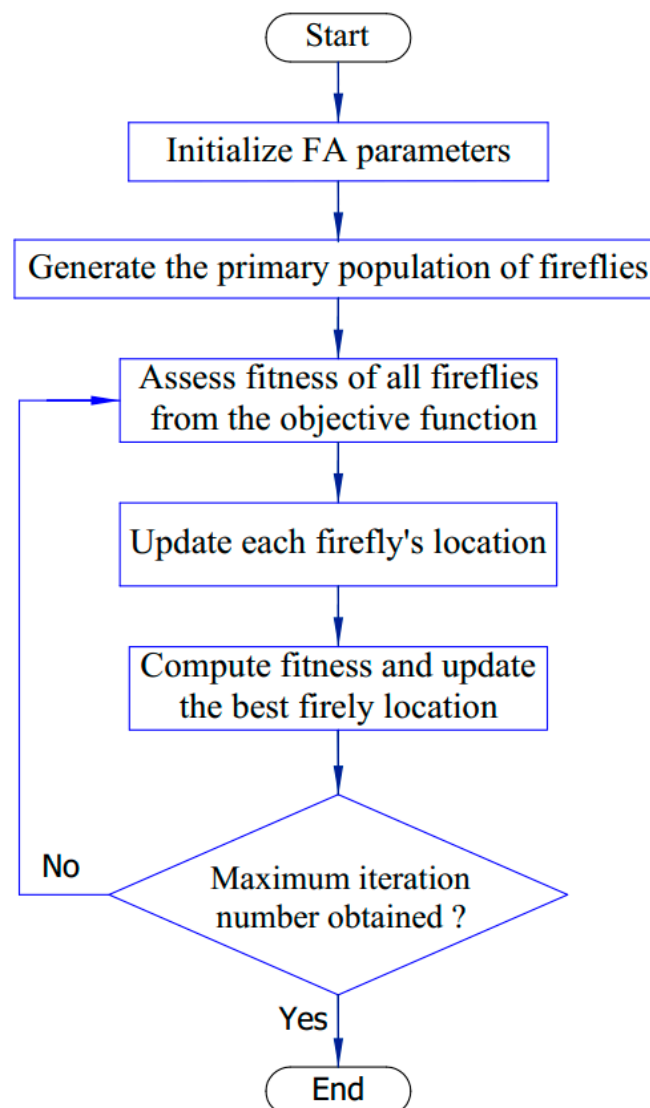


**Figure 8.** The flowchart of the Firefly algorithm.

## 4. Results and Discussion

### 4.1. Dynamic Establishment for 1-DOF Stage

The kinematic and dynamic modelling of the stage is built via the PRBM-based Lagrange method. The achieved results are verified by the finite element analysis. A diagram scheme of the PRBM for the stage is demonstrated in Figure 9.

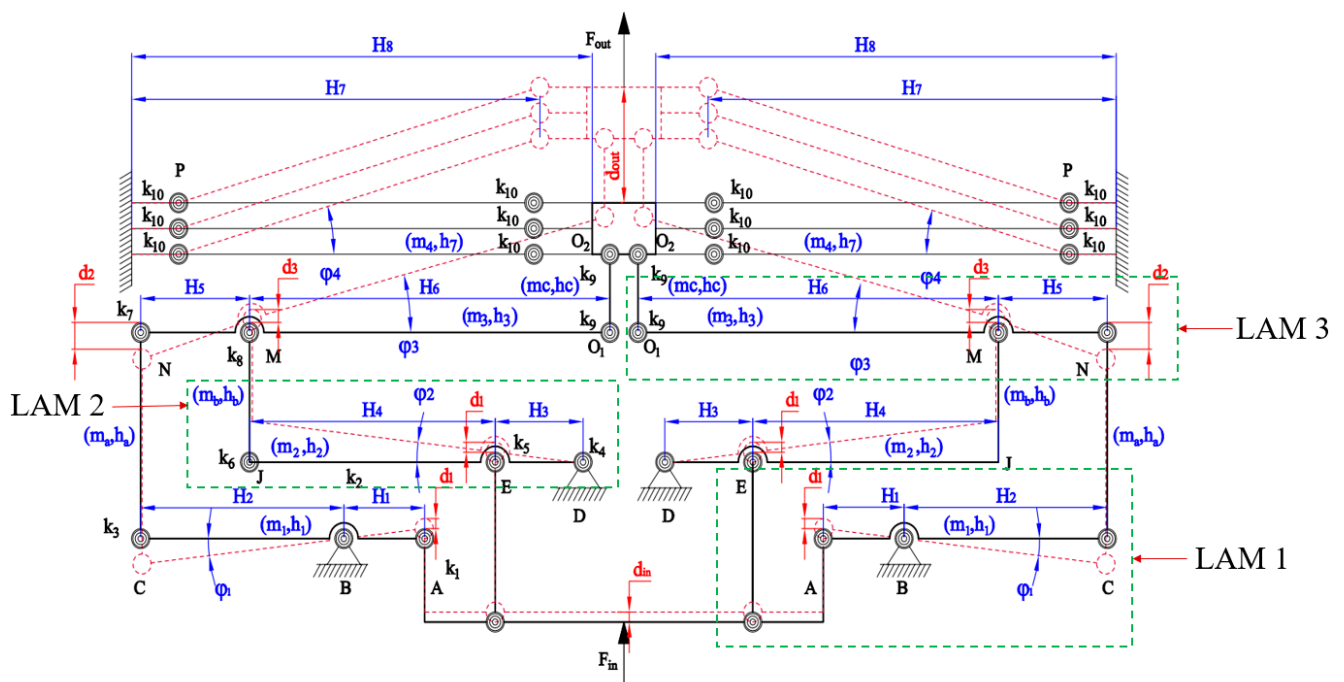


Figure 9. Pseudo-rigid-body diagram for the 1-DOF stage.

There are three main flexure hinges that are integrated into the proposed compliant 1-DOF stage. The main parameters of right circular hinge, elliptical hinge, and leaf hinge were illustrated in Figure 10, Figure 11, and Figure 12, respectively. In Figure 10, some of the main parameters include the thickness of the right circular hinge  $t_c$ , the radius of the right circular hinge ( $r$ ), and the width of the right circular hinge ( $b_c$ ). Figure 11 shows the thickness of the elliptical hinge ( $h$ ), the width of the elliptical hinge ( $w$ ), and the two semi-axes of the elliptical hinge ( $a$  and  $b$ ). In Figure 12,  $a_r$  is the thickness of the leaf hinge and  $b_r$  is the width of the leaf hinge.

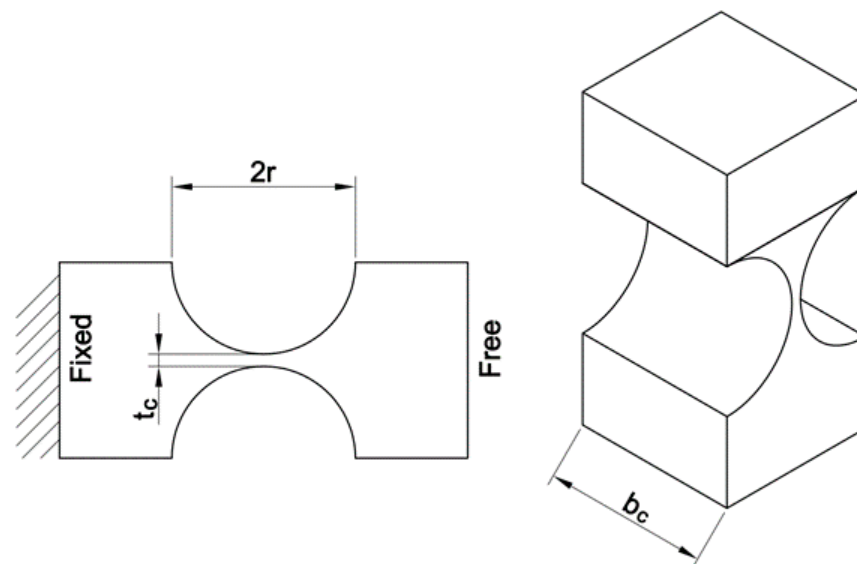


Figure 10. Main parameters of right circular hinge.

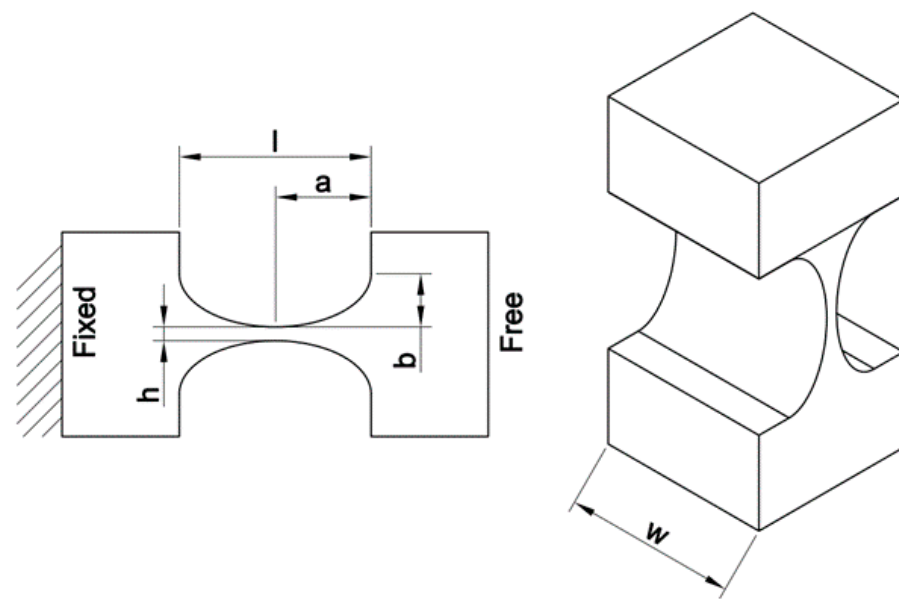


Figure 11. The main parameter of flexure elliptical hinge.

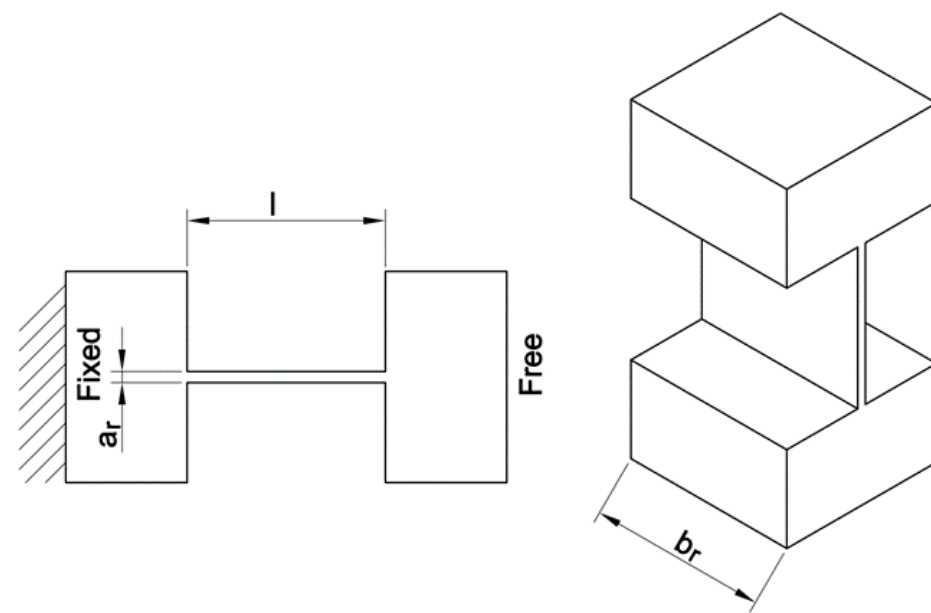


Figure 12. The main parameter of flexure leaf hinge.

As seen in Figures 4 and 9, the input displacements of LAM #1, LAM #2, and the output end consist of  $d_{in}$ ,  $d_{outC}$  and  $d_{outJ}$ , and  $d_{out}$ , respectively. The output displacement of LAM #1 and LAM #2 is the input displacement of the LAM #3. The dynamic equation of the stage is formed according to the chain of equations as:

$$d_{in} \frac{H_2}{H_1} = d_{outC} = d_2 \tag{6}$$

$$d_{in} \left( \frac{H_3 + H_4}{H_3} \right) = d_{outJ} = d_3 \tag{7}$$

$$d_{out} = d_2 \left( \frac{H_6}{H_5} \right) + d_3 \left( \frac{H_5 + H_6}{H_5} \right) \tag{8}$$

$$d_{out} = d_{in} \left( \frac{H_2 H_3 H_6 + H_1 (H_3 + H_4) (H_5 + H_6)}{H_1 H_3 H_5} \right) \tag{9}$$

$$AR = \frac{d_{out}}{d_{in}} = \frac{H_2 H_3 H_6 + H_1 (H_3 + H_4) (H_5 + H_6)}{H_1 H_3 H_5} \quad (10)$$

where  $m_i$  denotes the mass,  $H_i$  is the length, and  $\varphi_j$  ( $i = 1, 2 \dots 6, 7$ ), ( $j = 1, 2, 3, 4$ ) represents the rotary angular of the rigid links.

The torsional stiffness of the right circular hinge ( $K_C$ ) is described in Equation (11). The torsional stiffness of elliptical hinge ( $K_E$ ) is depicted in Equation (13). The torsional stiffness of leaf hinge ( $K_L$ ) is formed in Equation (14). The moment of inertia of the rigid links ( $I_j$ ) are described in Equation (15).

$$K_C = \frac{2Eb_c t_c^{2.5}}{9\pi r^{0.5}} \quad (11)$$

$$N_E = \frac{2 \left[ \sqrt{4\left(\frac{b}{h}\right) + 1} \left( 6\left(\frac{b}{h}\right)^2 + 4\left(\frac{b}{h}\right) + 1 \right) \right] + 6\left(\frac{b}{h}\right) \left( 2\left(\frac{b}{h}\right) + 1 \right)^2 \arctan \left( \sqrt{4\left(\frac{b}{h}\right) + 1} \right)}{\left( 2\left(\frac{b}{h}\right) + 1 \right) \left( 4\left(\frac{b}{h}\right) + 1 \right)^{5/2}} \quad (12)$$

$$K_E = \frac{Ewh^3}{6N_E l_e} \quad (13)$$

$$K_L = \frac{Ea^3b}{12I} \quad (14)$$

$$I_j = \frac{m_x H_j^2}{12} \quad (15)$$

In Figure 9, the kinetic energy of the proposed stage is defined by:

$$E_k = \sum_1^7 (E_t + E_r) = \sum_1^7 \left( \frac{1}{2} m_i v_i^2 + \frac{1}{2} I_i \dot{\varphi}_j^2 \right) \quad (16)$$

Using Equation (11), the kinetic energy of each rigid link/part is calculated as:

$$E_k = \frac{1}{2} m_1 \left( \frac{H_1 + H_2}{2} \dot{\varphi}_1 \right)^2 + \frac{1}{2} I_1 \dot{\varphi}_1^2 + \frac{1}{2} m_2 \left( \frac{H_3 + H_4}{2} \dot{\varphi}_2 \right)^2 + \frac{1}{2} I_2 \dot{\varphi}_2^2 + \frac{1}{2} m_a \left( \frac{H_1 + H_2}{2} \dot{\varphi}_1 \right)^2 + \frac{1}{2} m_b \left( (H_3 + H_4) \dot{\varphi}_2 \right)^2 + \frac{1}{2} m_3 \left( \frac{H_5 + H_6}{2} \dot{\varphi}_3 \right)^2 + \frac{1}{2} I_3 \dot{\varphi}_3^2 + \frac{1}{2} 3m_4 \left( \frac{H_7}{2} \dot{\varphi}_4 \right)^2 + \frac{1}{2} I_4 \dot{\varphi}_4^2 + \frac{1}{2} m_c \left( (H_5 + H_6) \dot{\varphi}_3 \right)^2 \quad (17)$$

In Figure 9, the elastic energy of the proposed stage is defined as:

$$E_V = \sum_{j=1}^4 \frac{1}{2} K_j \varphi_j^2 \quad (18)$$

The elastic energy that is achieved based on the deformation of the elliptical hinge, right circular hinge, and leaf hinge:

$$E_V = \frac{1}{2} (k_1 + k_2 + k_3) \varphi_1^2 + \frac{1}{2} (k_4 + k_5 + k_6) \varphi_2^2 + \frac{1}{2} (k_7 + k_8 + 2k_9) \varphi_3^2 + (6k_{10}) \varphi_4^2 \quad (19)$$

The rotation angular and angular velocity of every link are symbolled ( $\varphi_j, \dot{\varphi}_j$ ). The relationships between the rotary angulars are determined by:

$$\varphi_1 = \frac{d_{in}}{H_1} \quad (20)$$

$$\varphi_2 = \left( \frac{H_1}{H_3 + H_4} \right)^2 \varphi_1 \quad (21)$$

$$\varphi_3 = \left( \frac{(H_2H_3H_6 + H_1(H_3 + H_4)(H_5 + H_6))}{H_3H_5(H_5 + H_6)} \right) \varphi_1 \quad (22)$$

$$\varphi_4 = \left( \frac{(H_2H_3H_6 + H_1(H_3 + H_4)(H_5 + H_6))}{H_3H_5H_7} \right) \varphi_1 \quad (23)$$

By applying an input force  $F_{in}$ , the work is defined as:

$$W = \frac{1}{2} F_{in} d_{in} \quad (24)$$

Considering  $W = E_V$ , the input force and the input displacement have formed a relation as follows:

$$\frac{1}{2} F_{in} d_{in} = \frac{1}{2} \left[ \begin{array}{l} (k_1 + k_2 + k_3) \frac{1}{H_1^2} + (k_4 + k_5 + k_6) \frac{1}{(H_3 + H_4)^2} \\ + (k_7 + k_8 + 2k_9) \left( \frac{(H_2H_3H_6 + H_1(H_3 + H_4)(H_5 + H_6))}{H_1H_3H_5(H_5 + H_6)} \right) \\ + 6k_{10} \left( \frac{(H_2H_3H_6 + H_1(H_3 + H_4)(H_5 + H_6))}{H_1H_3H_5H_7} \right)^2 \end{array} \right] d_{in}^2 \quad (25)$$

If the input stiffness of the stage ( $K_{in} = F_{in}/d_{in}$ ) divides both sides by  $d_{in}^2$ , the stiffness is determined as:

$$K_{in} = (k_1 + k_2 + k_3) \frac{1}{H_1^2} + (k_4 + k_5 + k_6) \frac{1}{(H_3 + H_4)^2} + (k_7 + k_8 + 2k_9) \left( \frac{(H_2H_3H_6 + H_1(H_3 + H_4)(H_5 + H_6))}{H_1H_3H_5(H_5 + H_6)} \right) + 6k_{10} \left( \frac{(H_2H_3H_6 + H_1(H_3 + H_4)(H_5 + H_6))}{H_1H_3H_5H_7} \right)^2 \quad (26)$$

In the structure, the kinetic energy ( $E_k$ ) and the elastic energy ( $E_v$ ) may be conveyed. These two energies are assembled into Lagrange function as  $L = E_k - E_v$ .

$$\sum_{j=1}^4 \left\{ \frac{d}{dt} \left( \frac{\partial L}{\partial \dot{\varphi}_j} \right) - \frac{\partial L}{\partial \varphi_j} = Q_j \right\} \quad (27)$$

The equation of motion can be defined as follows:

$$\bar{M} \ddot{\varphi}_1 + \bar{K} \varphi_1 = 0 \quad (28)$$

$$\begin{aligned} \bar{M} = & m_1 \left( \frac{H_1 + H_2}{2} \right)^2 + I_1 + m_2 \left( \frac{H_1}{2} \right)^2 + I_2 \left( \frac{H_1}{H_3 + H_4} \right)^2 + m_a \left( \frac{H_1 + H_2}{2} \right)^2 + m_b (H_1)^2 + \\ & m_3 \left( \frac{(H_2H_3H_6 + H_1(H_3 + H_4)(H_5 + H_6))}{2H_3H_5} \right)^2 + I_3 \left( \frac{(H_2H_3H_6 + H_1(H_3 + H_4)(H_5 + H_6))}{H_3H_5(H_5 + H_6)} \right)^2 + \\ & 3m_4 \left( \frac{(H_2H_3H_6 + H_1(H_3 + H_4)(H_5 + H_6))}{2H_3H_5} \right)^2 + I_4 \left( \frac{(H_2H_3H_6 + H_1(H_3 + H_4)(H_5 + H_6))}{H_3H_5H_7} \right)^2 + \\ & m_c \left( \frac{(H_2H_3H_6 + H_1(H_3 + H_4)(H_5 + H_6))}{H_3H_5} \right)^2 \end{aligned} \quad (29)$$

$$\begin{aligned} \bar{K} = & (k_1 + k_2 + k_3) + (k_4 + k_5 + k_6) \left( \frac{H_1}{H_3 + H_4} \right)^2 + (k_7 + k_8 + 2k_9) \left( \frac{(H_2H_3H_6 + H_1(H_3 + H_4)(H_5 + H_6))}{H_3H_5(H_5 + H_6)} \right)^2 \\ & + 6k_{10} \left( \frac{(H_2H_3H_6 + H_1(H_3 + H_4)(H_5 + H_6))}{H_3H_5H_7} \right)^2 \end{aligned} \quad (30)$$

The first natural frequency of the proposed positioner is defined as the following equation:

$$f = \frac{1}{2\pi} \left( \frac{\bar{K}}{\bar{M}} \right)^{0.5} \quad (31)$$

which has the unit of Hertz.

#### 4.2. Verification of Established Analytical Models

The analytical results are validated using Finite element analysis (FEA). From the theory, the natural frequency was 176.96 Hz, and the first natural frequency was 195.07 Hz from the FEA results. As given in Table 2, the deviation error between the theory and the FEA test is about 9.28%. This means that that the formulated modelling method is a good enough and reliable approach to evaluate the initial characteristic of the developed stage.

**Table 2.** Validation for the analytical result through FEA result.

Response	Theory	FEA	Error (%)
$f$ (Hz)	176.96	195.07	9.28

#### 4.3. Parameter Optimization of 1-DOF Stage

To avoid the resonance phenomena between the motors, PZT actuators, and compliant 1-DOF stage, the first natural frequency modes are either as small as possible or as large as possible. In improving the rapid responsiveness of the positioners, the first natural frequency should be chosen as large as possible. In addition, the angular frequency is proportional to the natural frequency of the compliant stage. Therefore, the first natural frequency is proposed to maximize in order to increase the response speed as well as avoid the resonance phenomena of the positioner. In this article, the optimization problem is aimed to maximize the resonant frequency, which is briefly defined as:

Find design vector:  $\mathbf{x} = [x_1, x_2, x_3, x_4]$

$$\text{Maximize } f(\mathbf{x}) \quad (32)$$

S.t:

$$f(\mathbf{x}) > 200 \text{ Hz} \quad (33)$$

Limits of design variables (unit: mm):

$$\begin{cases} 0.65 \leq x_1 \leq 0.75 \\ 0.5 \leq x_2 \leq 0.7 \\ 0.5 \leq x_3 \leq 0.65 \\ 0.5 \leq x_4 \leq 0.6 \end{cases} \quad (34)$$

where  $f(\mathbf{x})$  symbolizes the resonant frequency. Meanwhile,  $x_1$ ,  $x_2$ ,  $x_3$ , and  $x_4$  are the dimensions  $R$ ,  $G$ ,  $S$ , and  $U$ , respectively. Especially, the range of design variables depends on the design experiences and the characteristics of different floors. Specifically, the thickness of floor 1 should be more than that of floor 2. In addition, the thickness of floor 2 should be more than that of floor 3. This is needed to permit the strength of the proposed stage as well as reduce the loss of displacement energy. Meanwhile, a suitable thickness of various positions of different floors should be defined by optimization process in order to find the most appropriate values for the proposed structure.

Based on Equations (2)–(34), MATLAB 2017 was employed to develop the integration approach of the PRBM method and Lagrange's principle, and the Firefly algorithm. As a result, the optimal parameters of the stage were found at  $G = 0.75$  mm,  $R = 0.7$  mm,  $S = 0.65$  mm,  $U = 0.6$  mm. The results found that the first natural frequency is approximately 226.8458 Hz. The convergence of the proposed algorithm is provided in Figure 13.

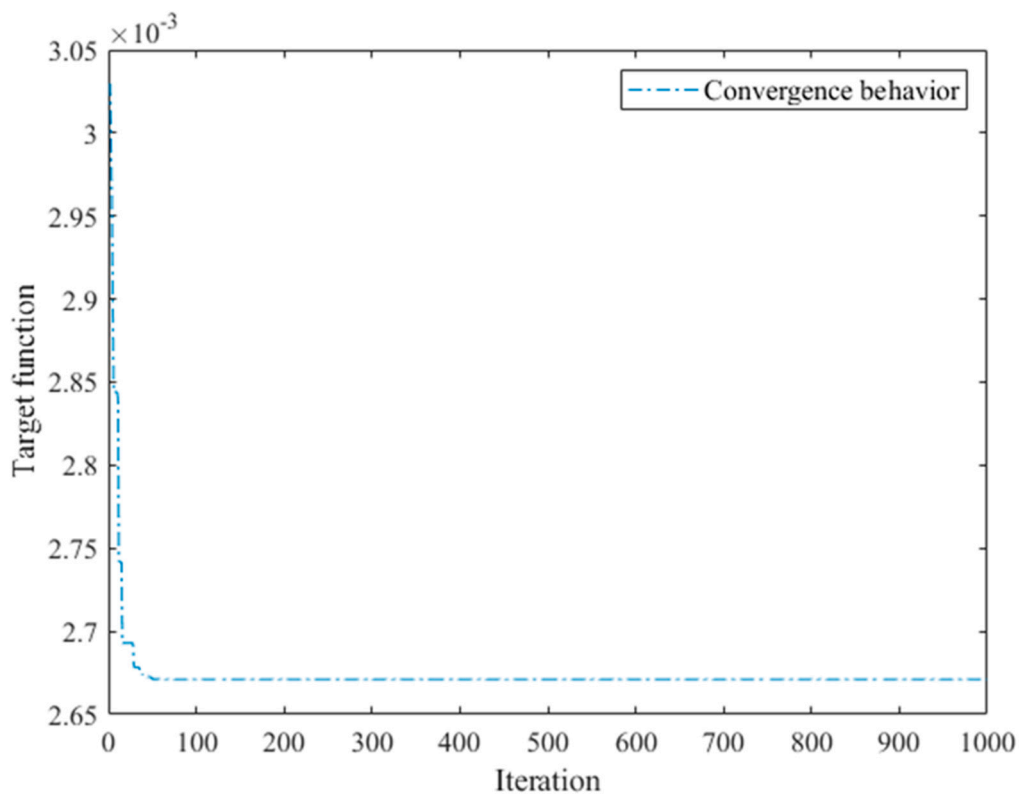


**Figure 13.** Convergence plot of the proposed algorithm.

In addition, a parametric/sensitive study was performed to demonstrate the influences of the design variables on the first natural frequency, the output displacement, and the safety factor. This work is performed based on the response surface method and FEA. The effects of the variable parameters on the first natural frequency, the output displacement, and the safety factor are provided in Figure 14a–e, Figure 15a–e, and Figure 16a–e, respectively.

#### 4.4. FEA Validation and Comparison

The optimized parameters were used to draw a 3D model. The FEA results showed that the first natural frequency was 250.01 Hz. In comparison with the draft design result, the frequency of the developed stage was improved up to 28.19%, as given in Table 3. In addition, the error optimal results and the FEA results for the first natural frequency was 9.27%, as illustrated in Table 4. This means that the presented method framework is a reliable tool for modeling the stage. Furthermore, the resonant frequency worth of six modes (1–6) are 250.01 Hz, 846.6 Hz, 897.53 Hz, 1146.6 Hz, 1305 Hz, and 1392.3 Hz, correspondingly. Figure 17 demonstrates the first natural frequency of the 01-DOF stage. Therefore, the above-mentioned resonant frequency values should be considered in order to evade the damage of the proposed stage.

**Table 3.** Comparison of the optimized design with the draft design.

Response	Optimal Result	Initial Design Result	Improvement (%)
$f$ (Hz)	226.8458	176.96	28.19

**Table 4.** Verification of the optimized result by FEA.

Response	Optimal Design	Simulation	Error (%)
$f$ (Hz)	226.8458	250.01	9.27

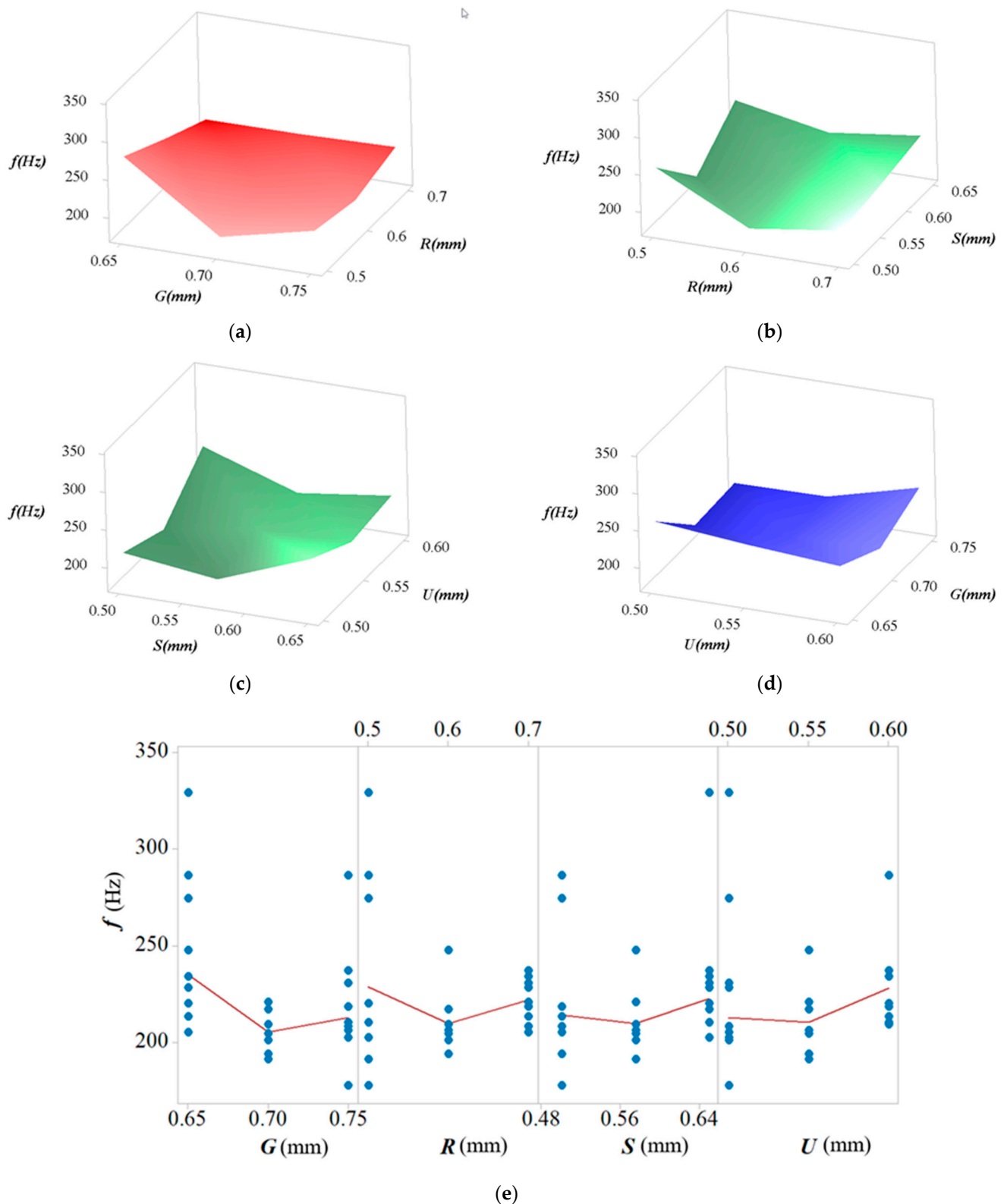


**Figure 14.** Trends of the frequency based on the alteration of the key stage dimensions: (a) first natural frequency with factors  $G$  and  $R$ , (b) first natural frequency with factors  $R$  and  $S$ , (c) first natural frequency with factors  $S$  and  $U$ , (d) first natural frequency with factors  $U$  and  $R$ , and (e) first natural frequency with factors  $G$ ,  $R$ ,  $S$ , and  $U$ .

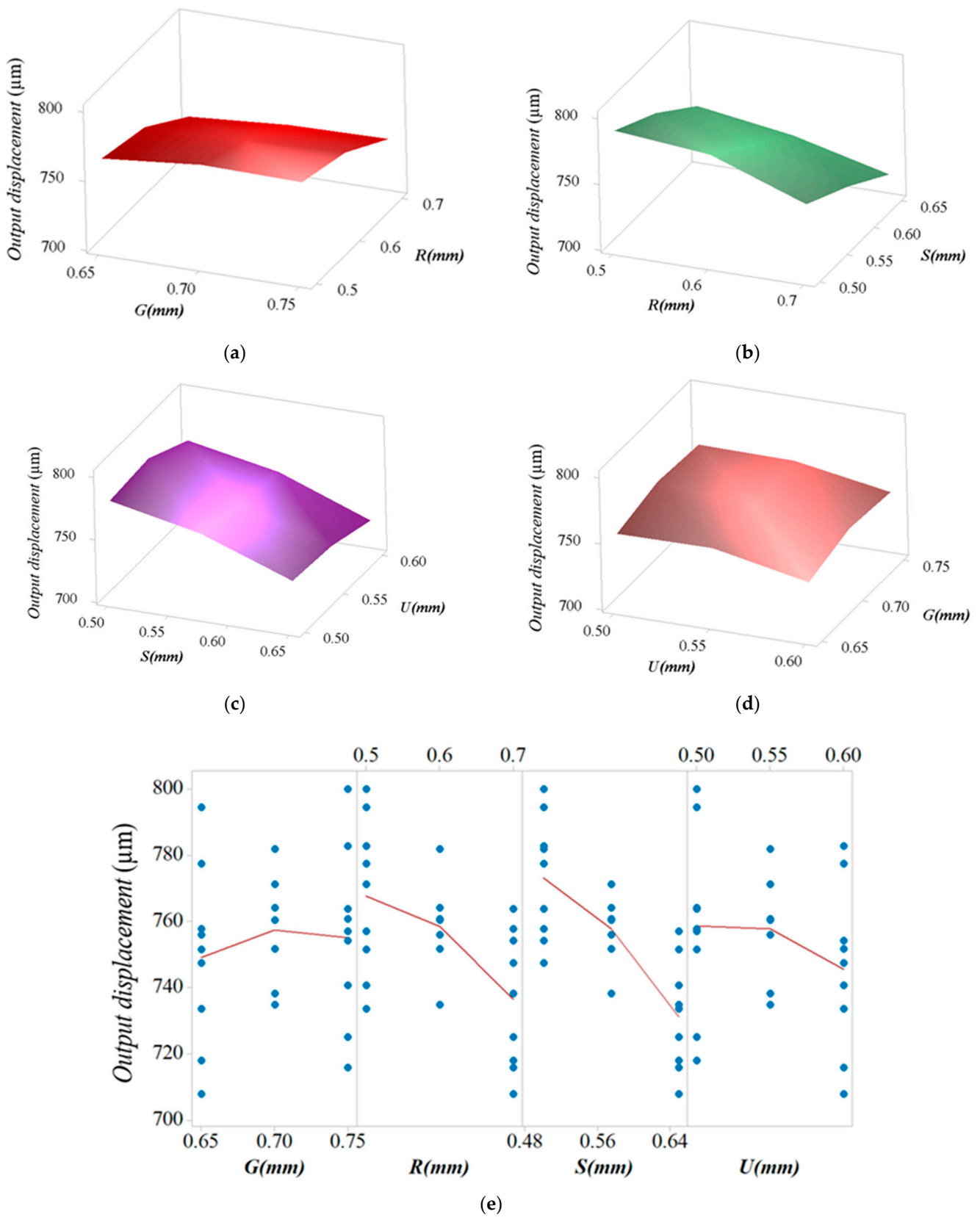


**Figure 15.** Trends of the output displacement (input displacement of  $52 \mu\text{m}$ ) based on the alteration of the key stage dimensions: (a) output displacement versus  $G$  and  $R$ , (b) output displacement versus  $R$  and  $S$ , (c) output displacement versus  $S$  and  $U$ , (d) output displacement versus  $U$  and  $R$ , and (e) output displacement versus  $G$ ,  $R$ ,  $S$ , and  $U$ .

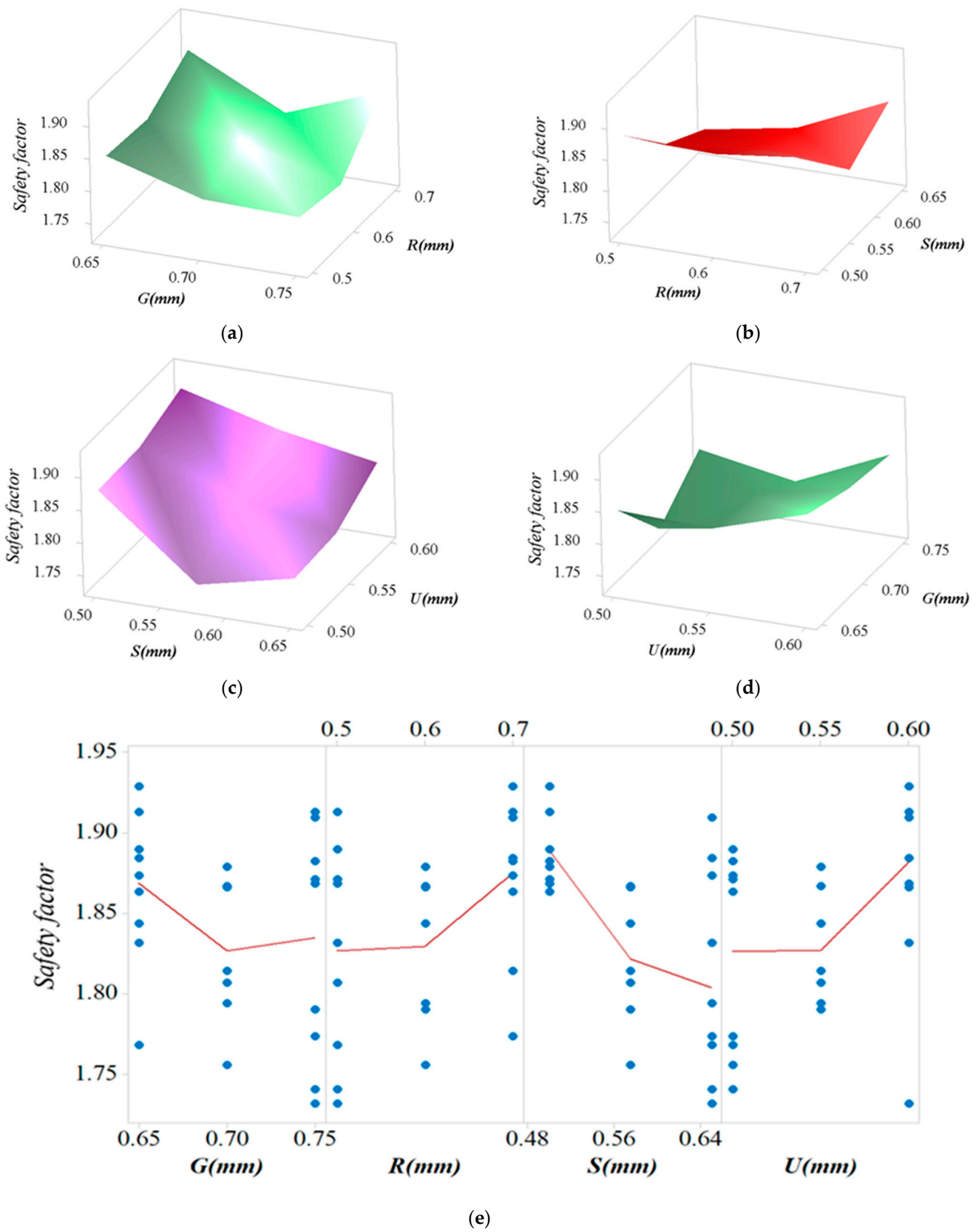


**Figure 16.** Trends of the safety factor (input displacement of 52  $\mu m$ ) based on the alteration of the key stage dimensions: (a) safety factor with factors  $G$  and  $R$ , (b) safety factor with factors  $R$  and  $S$ , (c) safety factor with factors  $S$  and  $U$ , (d) safety factor with factors  $U$  and  $R$ , and (e) safety factor with factors  $G$ ,  $R$ ,  $S$ , and  $U$ .

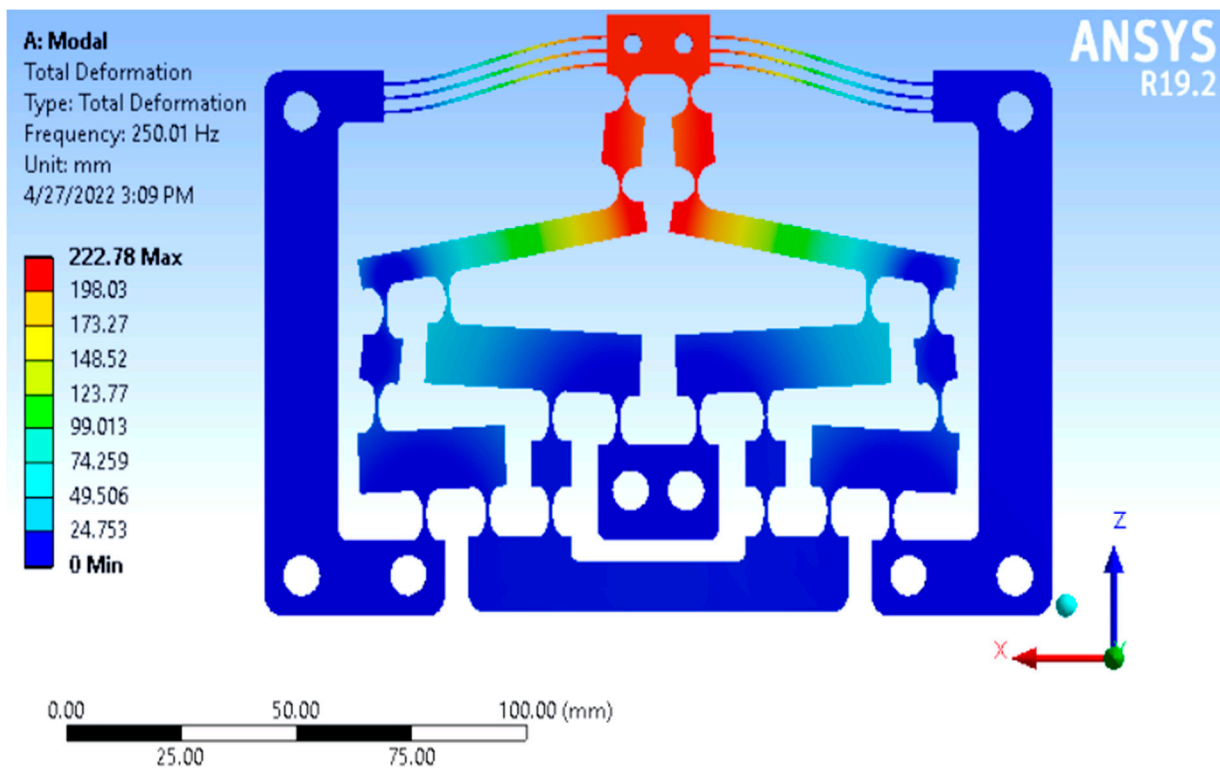


Figure 17. The frequency result of the optimized stage.

In this work, the Skewness criterion was employed to define the mesh quality. The results found that the average value of this criterion was about 0.66, as given in Figure 18. This value ensures a good mesh for the stage during the simulation.

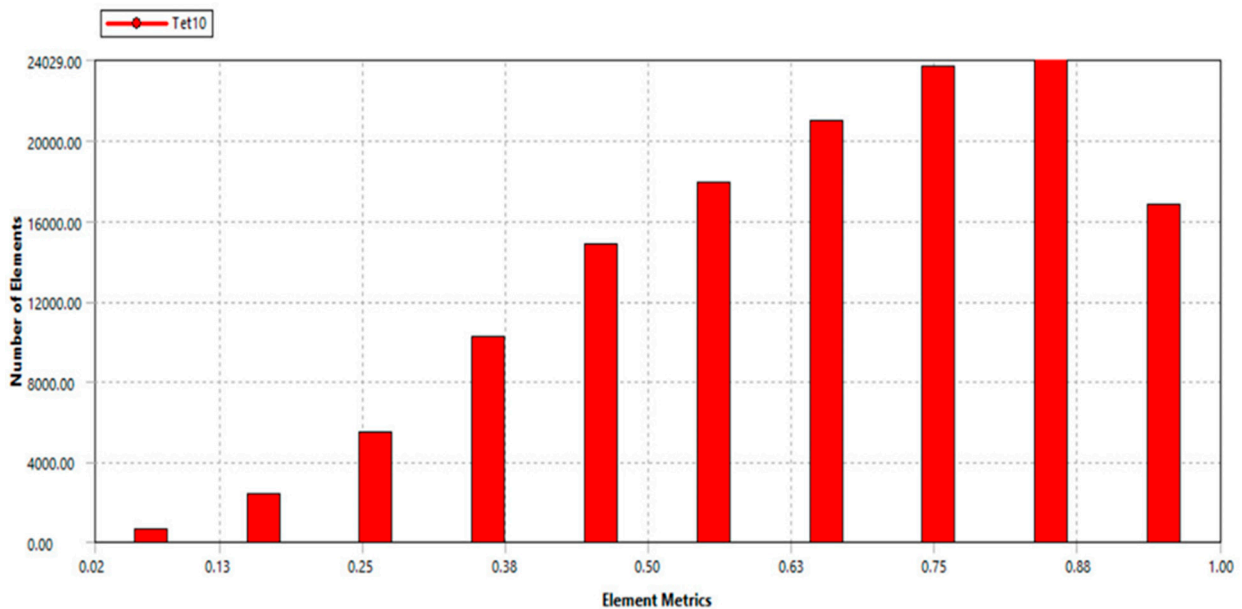


Figure 18. Skewness criteria for the meshing quality.

In comparison with other optimization methods, the proposed method was compared with the differential evolutionary algorithm (DE) [35] and neural network algorithm (NNA) [36]. The achieved frequency from the present method and two DE and NNA were almost similar, as given in Table 5.

**Table 5.** Comparison between the presented method and other methods.

Response	Presented Method	DE	NNA
$f$ (Hz)	226.8458	226.8456	226.8448

Table 6 provides a comparison of the present design with the several existing designs. The results found that the frequency of the present stage is superior to others.

**Table 6.** Comparison of the present design with previous designs.

Studies	Dimensions	First-Order Resonant Frequency (Hz)
Xu [37]	100 mm × 100 mm × 10 mm	91.97
Li and Tian [38]	NA	192.00
Chau et al. [39]	120 mm × 50 mm × 10 mm	79.517
The proposed design	<b>171 mm × 108 mm × 10 mm</b>	<b>250.01</b>

## 5. Conclusions

This article developed a new design of the 01-DOF stage. It was designed to include the six-lever displacement amplifier and the parallel guiding mechanism. An efficient integration of the PRBM-based Lagrange method was to build the dynamic equation of the 1-DOF stage. Based on the analytical equation, the Firefly algorithm was implemented to define the optimal parameters.

The optimized parameters were found at  $G = 0.75$  mm,  $R = 0.7$  mm,  $S = 0.65$  mm, and  $U = 0.6$  mm. The optimized first natural frequency was about 226.8458 Hz. In addition, the FEA verification results showed that the first natural frequency was 250.01 Hz. Moreover, the verification error among the optimization and FEA results was 9.27%. The simulation verification was close with the optimal result from the hybrid approach. Moreover, the optimization result was better than the primary design.

In the future investigations, some prototypes will be fabricated based on the additive manufacturing method or computerized wire cutting method for evaluating with the numerical analysis and analytical calculation results. A practical manufacture of the stage will be embedded into a development of an in situ nanoindentation device.

**Author Contributions:** Conceptualization, M.P.D. and H.G.L.; Methodology, M.P.D. and T.-P.D.; Software, M.P.D. and N.T.D.T.; Validation, M.P.D. and H.G.L.; Formal Analysis, M.P.D.; Investigation, M.P.D. and T.-P.D.; Data Curation, M.P.D.; Writing—original draft preparation, M.P.D. and N.T.D.T.; writing—review and editing, H.G.L., N.L.C. and T.-P.D. All authors have read and agreed to the published version of the manuscript.

**Funding:** This work belongs to the project grant No: T2021-10TĐ, funded by Ho Chi Minh City University of Technology and Education, Vietnam.

**Institutional Review Board Statement:** Not applicable.

**Informed Consent Statement:** Not applicable.

**Data Availability Statement:** The data used to support the findings of this study are included within the article.

**Conflicts of Interest:** The authors declare that they have no conflict of interest.

## Nomenclature

1-DOF	One degree of freedom
SEM	Scanning electron microscope
TEM	Transmission electron microscope
PRBM	Pseudo-rigid-body model
ANFIS	Adaptive neuro-fuzzy inference system
PZT	Piezoelectric actuator
LAM 1	Lever displacement amplifier of floor 1
LAM 2	Lever displacement amplifier of floor 2
LAM 3	Lever displacement amplifier of floor 3
$K_C$	Stiffness of the semi-circular flexural hinge
$K_E$	Stiffness of elliptical hinge
$K_L$	Stiffness of leaf hinge
FEA	Finite element analysis
DE	Differential evolutionary algorithm
NNA	Neural network algorithm
$f$	First natural frequency

## References

- Nowak, J.D.; Rzepiejewska-Malyska, K.A.; Major, R.C.; Warren, O.L.; Michler, J. In-situ nanoindentation in the SEM. *Mater. Today* **2010**, *12*, 44–45. [\[CrossRef\]](#)
- Ebenstein, D.M.; Pruitt, L.A. Nanoindentation of biological materials. *Nano Today* **2006**, *1*, 26–33. [\[CrossRef\]](#)
- Alderete, N.; Zaheri, A.; Espinosa, H. A Novel In Situ Experiment to Investigate Wear Mechanisms in Biomaterials. *Exp. Mech.* **2019**, *59*, 659–667. [\[CrossRef\]](#)
- Hu, Z.; Lynne, K.J.; Markondapatnaikuni, S.P.; Delfanian, F. Material elastic–plastic property characterization by nanoindentation testing coupled with computer modeling. *Mater. Sci. Eng. A* **2013**, *587*, 268–282. [\[CrossRef\]](#)
- O’Brien, W. Long-range motion with nanometer precision. *Photonics Spectra* **2005**, *39*, 80–81.
- Rabe, R.; Breguet, J.-M.; Schwaller, P.; Stauss, S.; Haug, F.-J.; Patscheider, J.; Michler, J. Observation of fracture and plastic deformation during indentation and scratching inside the scanning electron microscope. *Thin Solid Films* **2004**, *470*, 206–213. [\[CrossRef\]](#)
- Ding, B.; Li, Y.; Xiao, X.; Tang, Y.; Li, B. Design and analysis of a 3-DOF planar micromanipulation stage with large rotational displacement for micromanipulation system. *Mech. Sci.* **2017**, *8*, 117–126. [\[CrossRef\]](#)
- Jiang, C.; Lu, H.; Zhang, H.; Shen, Y.; Lu, Y. Recent Advances on In Situ SEM Mechanical and Electrical Characterization of Low-Dimensional Nanomaterials. *Scanning* **2017**, *2017*, 1985149. [\[CrossRef\]](#)
- Gianola, D.S.; Sedlmayr, A.; Mönig, R.; Volkert, C.A.; Major, R.C.; Cyrankowski, E.; Asif, S.A.S.; Warren, O.L.; Kraft, O. In situ nanomechanical testing in focused ion beam and scanning electron microscopes. *Rev. Sci. Instrum.* **2011**, *82*, 063901. [\[CrossRef\]](#)
- Haque, M.; Saif, M. Application of MEMS force sensors for in situ mechanical characterization of nano-scale thin films in SEM and TEM. *Sens. Actuators A Phys.* **2002**, *97–98*, 239–245. [\[CrossRef\]](#)
- Lu, Y.; Ganesan, Y.; Lou, J. A Multi-step Method for In Situ Mechanical Characterization of 1-D Nanostructures Using a Novel Micromechanical Device. *Exp. Mech.* **2009**, *50*, 47–54. [\[CrossRef\]](#)
- Xu, Q. Design and testing of a novel multi-stroke micropositioning system with variable resolutions. *Rev. Sci. Instrum.* **2014**, *85*, 025002. [\[CrossRef\]](#) [\[PubMed\]](#)
- Lu, K.; Zhang, J.; Chen, W.; Jiang, J.; Chen, W. A monolithic microgripper with high efficiency and high accuracy for optical fiber assembly. In Proceedings of the 9th IEEE Conference on Industrial Electronics and Applications, Hangzhou, China, 9–11 June 2014; pp. 1942–1947. [\[CrossRef\]](#)
- Putra, A.S.; Huang, S.; Tan, K.K.; Panda, S.K.; Lee, T.H. Design, modeling, and control of piezoelectric actuators for intracytoplasmic sperm injection. *IEEE Trans. Control Syst. Technol.* **2007**, *15*, 879–890. [\[CrossRef\]](#)
- Huang, H.; Zhao, H.; Mi, J.; Yang, J.; Wan, S.; Xu, L.; Ma, Z. A novel and compact nanoindentation device for in situ nanoindentation tests inside the scanning electron microscope. *AIP Adv.* **2012**, *2*, 012104. [\[CrossRef\]](#)
- Huang, H.; Zhao, H.; Mi, J.; Yang, J.; Wan, S.; Yang, Z.; Yan, J.; Ma, Z.; Geng, C. Experimental research on a modular miniaturization nanoindentation device. *Rev. Sci. Instrum.* **2011**, *82*, 095101. [\[CrossRef\]](#) [\[PubMed\]](#)
- Zhao, H.; Huang, H.; Fan, Z.; Yang, Z.; Ma, Z. Design, Analysis and Experiments of a Novel in situ SEM Indentation Device. In *Nanoindentation in Materials Science*; IntechOpen: London, UK, 2012. [\[CrossRef\]](#)
- Dang, M.P.; Le, H.G.; Le Chau, N.; Dao, T.-P. A multi-objective optimization design for a new linear compliant mechanism. *Optim. Eng.* **2019**, *21*, 673–705. [\[CrossRef\]](#)
- Wang, P.; Xu, Q. Design of a flexure-based constant-force XY precision positioning stage. *Mech. Mach. Theory* **2017**, *108*, 1–13. [\[CrossRef\]](#)

20. Fan, S.; Liu, H.; Fan, D. Design and development of a novel monolithic compliant XY stage with centimeter travel range and high payload capacity. *Mech. Sci.* **2018**, *9*, 161–176. [[CrossRef](#)]
21. Wadikhaye, S.; Yong, Y.; Moheimani, S. Design of a compact serial-kinematic scanner for high-speed atomic force microscopy: An analytical approach. *Micro Nano Lett.* **2012**, *7*, 309–313. [[CrossRef](#)]
22. Gauthier, M.; Piat, E. Control of a particular micro-macro positioning system applied to cell micromanipulation. *IEEE Trans. Autom. Sci. Eng.* **2006**, *3*, 264–271. [[CrossRef](#)]
23. Ding, B.; Yang, Z.-X.; Zhang, G.; Xiao, X. Optimum design and analysis of flexure-based mechanism for non-circular diamond turning operation. *Adv. Mech. Eng.* **2017**, *9*, 1687814017743353. [[CrossRef](#)]
24. Ding, B.; Yang, Z.-X.; Xiao, X.; Zhang, G.; Yangd, Z.-X. Design of Reconfigurable Planar Micro-Positioning Stages Based on Function Modules. *IEEE Access* **2019**, *7*, 15102–15112. [[CrossRef](#)]
25. Ding, B.; Zhao, J.; Li, Y. Design of a spatial constant-force end-effector for polishing/deburring operations. *Int. J. Adv. Manuf. Technol.* **2021**, *116*, 3507–3515. [[CrossRef](#)]
26. Deng, L.; Ling, M. Design and integrated stroke sensing of a high-response piezoelectric direct-drive valve enhanced by push–pull compliant mechanisms. *Rev. Sci. Instrum.* **2022**, *93*, 035008. [[CrossRef](#)] [[PubMed](#)]
27. Kim, H.-Y.; Ahn, D.-H.; Gweon, D.-G. Development of a novel 3-degrees of freedom flexure based positioning system. *Rev. Sci. Instrum.* **2012**, *83*, 055114. [[CrossRef](#)]
28. Wang, F.; Liang, C.; Tian, Y.; Zhao, X.; Zhang, D. Design and Control of a Compliant Microgripper With a Large Amplification Ratio for High-Speed Micro Manipulation. *IEEE/ASME Trans. Mechatron.* **2016**, *21*, 1262–1271. [[CrossRef](#)]
29. Chang, S.H.; Du, B.C. A precision piezodriven micropositioner mechanism with large travel range. *Rev. Sci. Instrum.* **1998**, *69*, 1785–1791. [[CrossRef](#)]
30. Ling, M.; Howell, L.L.; Cao, J.; Chen, G. Kinetostatic and Dynamic Modeling of Flexure-Based Compliant Mechanisms: A Survey. *Appl. Mech. Rev.* **2020**, *72*, 030802. [[CrossRef](#)]
31. Le Chau, N.; Tran, N.T.; Dao, T.-P. Topology and size optimization for a flexure hinge using an integration of SIMP, deep artificial neural network, and water cycle algorithm. *Appl. Soft Comput.* **2021**, *113*, 108031. [[CrossRef](#)]
32. Dang, M.P.; Le, H.G.; Le, N.N.T.; Le Chau, N.; Dao, T.-P. Multiresponse Optimization for a Novel Compliant Z-Stage by a Hybridization of Response Surface Method and Whale Optimization Algorithm. *Math. Probl. Eng.* **2021**, *2021*, 9974230. [[CrossRef](#)]
33. Dang, M.P.; Le, H.G.; Le Chau, N.; Dao, T.-P. Optimization for a Flexure Hinge Using an Effective Hybrid Approach of Fuzzy Logic and Moth-Flame Optimization Algorithm. *Math. Probl. Eng.* **2021**, *2021*, 6622655. [[CrossRef](#)]
34. Yang, X.S.; He, X. Firefly algorithm: Recent advances and applications. *Int. J. Swarm Intell.* **2013**, *1*, 36–50. [[CrossRef](#)]
35. Yildiz, A.R. Hybrid Taguchi-differential evolution algorithm for optimization of multi-pass turning operations. *Appl. Soft Comput.* **2013**, *13*, 1433–1439. [[CrossRef](#)]
36. Dinh, V.B.; Le Chau, N.; Le, N.T.P.; Dao, T.-P. Topology-based geometry optimization for a new compliant mechanism using improved adaptive neuro-fuzzy inference system and neural network algorithm. *Eng. Comput.* **2021**, 1–30. [[CrossRef](#)]
37. Xu, Q. Design, testing and precision control of a novel long-stroke flexure micropositioning system. *Mech. Mach. Theory* **2013**, *70*, 209–224. [[CrossRef](#)]
38. Li, X.; Tian, Y. The design and new controller of a 1-DOF precision positioning platform. In Proceedings of the 2013 International Conference on Manipulation, Manufacturing and Measurement on the Nanoscale, Suzhou, China, 26–30 August 2013; pp. 190–194. [[CrossRef](#)]
39. Le Chau, N.; Tran, N.T.; Dao, T.-P. An Optimal Design Method for Compliant Mechanisms. *Math. Probl. Eng.* **2021**, *2021*, 5599624. [[CrossRef](#)]